Applied Catalysis B: Environmental 311 (2022) 121372

Contents lists available at ScienceDirect

Applied Catalysis B: Environmental

journal homepage: www.elsevier.com/locate/apcatb

Plasma-induced hierarchical amorphous carbon nitride nanostructure with two $N_{2\ C}$-site vacancies for photocatalytic H_2O_2 production

Yanmei Zheng [a,1], Yi Luo [a,1], Qiushi Ruan [a], Shaohua Wang [a], Jin Yu [a], Xinli Guo [a,*], Weijie Zhang [a], Hang Xie [a], Zheng Zhang [a], Ying Huang [b,*]

[a] Jiangsu Key Laboratory of Advanced Metallic Materials, School of Materials Science and Engineering, Southeast University, Nanjing 211189, China
[b] School of Energy and Environment, Southeast University, Nanjing 210096, China

ARTICLE INFO

Keywords:
Plasma treatment
Amorphous carbon nitride (ACN)
H_2O_2 production
Hierarchical nanostructure
N_{2C}-site vacancy
First-principles calculations

ABSTRACT

Carbon nitride (CN) with nitrogen vacancy is a robust photocatalyst with proven enhancing H_2O_2 production ability. However, nitrogen vacancy control is extremely challenging with the majority of reports representing it as a few vacancies. Herein, for the first time, the amorphous CN (ACN) with two $N_{2\ C}$-site vacancies in one CN unit is prepared by a one-step H_2 plasma approach. First-principles calculations and experimental results provide consistent evidence that two $N_{2\ C}$ vacancies are located in one CN unit structure after amorphous transformation. Plasma-induced ACN is stable with a hierarchical continuous nanosheet network structure and exhibits an ultrahigh specific surface area of ~405.76 m^2g^{-1}, which is 83 times higher than that of pristine CN (4.89 m^2g^{-1}) and significantly enhanced photocatalytic H_2O_2 production, yielding 1874 $\mu molg^{-1}h^{-1}$. Besides, the existence potential drop of 2.61 eV for the electrostatic potential in ACN is key to charge carrier separation. Moreover, the amorphous transformation leads to a new strong band tail, which remarkably enhances the absorbance edge of ACN up to 593 nm, resulting in a wider range of visible-light absorption to enhance H_2O_2 production. The results have provided an effective approach for promoting the practical application of ACN in photocatalytic H_2O_2 production.

1. Introduction

The prospect of converting sustainable solar energy into clean energy through photocatalysts has driven the search for efficient photocatalysts [1–4]. Among the photocatalysts explored, carbon nitride (CN) has become an extremely attractive visible light photocatalyst due to its nonmetallicity, nontoxicity, and stability [5,6]. However, bulk CN (BCN) still lacks satisfactory photocatalytic efficiency due to its limited visible light harvesting capacity, low charge transfer rate and low specific surface area [6–8]. Recently, the nanostructure tuning, amorphization and vacancy generation of CN have attracted increasing interest for improving its photocatalytic performance [9–11]. Notably, 2D CN nanosheets have been widely studied and can provide abundant active sites, short charge diffusion distances, enhance specific surface areas and promote the redox ability of photogenerated electrons and holes [10, 12]. However, 2D CN nanosheets have two fatal problems, which severely limits their practical application in solar energy conversion [13]. One is that the nanosheets easily agglomerate, which reduces the specific surface area. Second, due to the decrease in conjugation length and strong quantum confinement effect (QCE) [14], the band gap of CN nanosheets will increase greatly.

Recently, Xie et al. reported that a stable nanosheet structure without agglomeration can be obtained by the construction of a hierarchical structure since the hierarchical structure can reduce the embedding of nanomaterials, providing a large specific surface area and abundant pores [15–17]. However, hierarchical 2D CN nanosheets still suffer from unsatisfactory large bandgap. Thus, various modification approaches, such as element doping, construction heterojunctions/homojunctions and cocatalysts, are adopted to narrow the bandgap. Theoretically and experimentally, a most remarkable advantage of amorphous semiconductors is that the bandgaps are much smaller than their crystalline phase originated from their strong band tails due to N-defects induced intra-band energy levels [18]. It can effectively overcome the problem of increased bandgap for 2D nanosheets. Amorphous structures have

* Corresponding authors.
E-mail addresses: guo.xinli@seu.edu.cn (X. Guo), huangying@seu.edu.cn (Y. Huang).
[1] These authors contributed equally

https://doi.org/10.1016/j.apcatb.2022.121372
Received 26 October 2021; Received in revised form 15 March 2022; Accepted 2 April 2022
Available online 5 April 2022
0926-3373/© 2022 Elsevier B.V. All rights reserved.

strong band tails due to their asymmetric structure, which allows them to have a wider range of light absorption and thus harvest a greater proportion of solar radiation. This is a prerequisite for reducing bandgap [[19,20] Therefore, the exploration of high-efficiency amorphous CN (ACN) photocatalysts is still desirable but challenging [21]. To date, there are only a few reports about ACN photocatalysis, and there are especially no reports on photocatalytic H_2O_2 production, which can be confirmed in Table S1, Supporting Information. Additionally, most reports have focused on destroying the short-range order structure by introducing foreign atoms to obtain ACN [22–24]. However, the introduction of foreign metal elements will affect the nonmetallic properties of CN. Therefore, the exploration of pure ACN photocatalysts completely composed of C and N is still challenging. Plasma, as a high-energy particulate matter composed of ions, electrons, and unionized neutral particles, is widely used for the functionalization of CN materials to introduce carbon and/or nitrogen vacancies [25,26]. The CN with $N_{2\ C}$ (sp^2-hybridized nitrogen, C-N═C) vacancies has been proven to be significantly effective in photocatalytic H_2O_2 production, [27–29] but the mechanism is still unclear, and it is difficult to control vacancy generation and determination.

Herein, we report a one-step H_2 plasma treatment to induce a hierarchical ACN nanostructure with two $N_{2\ C}$-site vacancies in one unit of CN structure without foreign element doping. Plasma-induced ACN is stable with a hierarchical continuous nanosheet network structure and exhibits a narrowed bandgap as well as a strong band tail, which simultaneously solves fatal problems for 2D nanosheets of nanomaterial agglomeration, increased band gap and limited visible light harvesting capacity. Furthermore, ACN exhibits significantly enhanced photocatalytic H_2O_2 production yielding, owing to the fast charge carrier separation rate caused by the potential drop. The results have provided an effective approach for promoting the practical application of ACN in photocatalytic H_2O_2 production.

2. Experimental section

2.1. Synthesis of hierarchical Amorphous carbon nitride (ACN)

First, 2.5 g melamine and 2.55 g cyanuric acid were dissolved in 10 mL of concentrated sulfuric acid (H_2SO_4). Then, 1 g of $KMnO_4$ was added to the above mixed colloid in an ice bath. Subsequently, the mixed colloid was heated at 35 ℃ for 2 h and then 98 ℃ for 90 min. Later, 20 mL of H_2O_2 was added dropwise to remove residual $KMnO_4$. The precursor of melamine-cyanuric acid supramolecular (MCS) was obtained after centrifugation, washing with distilled water and drying at 80 ℃ for 48 h. The MCS was then treated in H_2 plasma under a pressure of 150 Pa in a H_2 flow rate of 30 sccm and a temperature of 400 ℃ for 90 min to induce hierarchical ACN. For comparison, the MCS was calcined at 550 ℃ for 2 h in a muffle furnace to obtain graphical carbon nitride labeled GCN. Bulk CN (BCN) was typically synthesized by calcining 5 g of melamine at 550 ℃ for 2 h in a muffle furnace.

2.2. Characterizations

The XRD patterns were recorded on a Bruker D8-Discover instrument to identify the crystal structure using Cu-K_α radiation. The microstructures and morphologies of samples were studied by scanning electron microscopy (SEM, FEI Inspect F50) and transmission electron microscopy (TEM, Titan 80–300). The Brunauer–Emmett–Teller surface area (BET, ASAP 2020) was calculated based on the nitrogen adsorption desorption isotherm. The characterization of compounds was recorded by Fourier transform infrared spectroscopy (FTIR, Nicolet 5700 Fourier-IR spectrometer) and X-ray photoelectron microscopy (XPS, PHI 500). Solid-state ^{13}C MAS NMR spectra were taken on a Bruker Advance III HD 400 MHz. Roman spectra (Lab RAM HR UV–Visible) were excited by a 325 nm laser with a 60 s integration time. Electron paramagnetic resonance (EPR, Bruker A300) and UV–vis absorbance spectra were measured by a digital X-band spectrometer and a Shimadzu UV-2550 UV–vis spectrometer, respectively. The Xe lamp was used as the excitation source when recorded on the photoluminescence (PL) spectra. The temperature-programmed desorption (TPD, BETCAT-A, Japan) of O_2 were carried out in He atmosphere at a heating rate of 10 °C/min up to 450 °C. The gas flow rate was 50 mL min^{-1}.

2.3. Photoelectrochemical measurement

Photoelectrochemical measurements were recorded on an electrochemical workstation (CHI660E, Shanghai, China) in a three-electrode system. The obtained photocatalysts, saturated Ag/AgCl and platinum foil were used as the working photoelectrode, reference electrode and counter electrode, respectively. The working photoelectrode was prepared by dispersing 1 mL of N, N-dimethylformamide (DMF), 40 μL of Nafion and 5 mg photocatalyst under sonication. Afterwards, 20 μL of the obtained suspension was dropped onto ITO with an area of 1 cm^2. Then, the working photoelectrode was dried at room temperature overnight. The tests were conducted using a 300 W xenon lamp (PLS-SXE 300D/300DUV, Beijing Perfect light) as the light source in an irradiation reaction vessel containing 0.1 M Na_2SO_4 solution.

2.4. Photocatalytic hydrogen peroxide production and decomposition

Photocatalytic H_2O_2 production experiments were used to characterize the photocatalytic activity. Typically, 25 mg of photocatalyst was dissolved in 50 mL of 10% isopropanol (IPA) solution. O_2 was bubbled into the mixed solution for 30 min to ensure adsorption-desorption equilibrium before irradiation. Then, the mixed solution was exposed to a 300 W xenon lamp with bubbling O_2 flow. At regular intervals, 1.5 mL of the reaction solution was taken and centrifuged to obtain the supernatant. The H_2O_2 concentration was measured by the normal iodometric method[25,30,31], and the standard H_2O_2 concentration working curve is shown in (Fig. S1, Supporting Information).

The photocatalytic decomposition of H_2O_2 was conducted in an H_2O_2, O_2-saturated and simulated sunlight irradiation system. First, 25 mg of the catalyst was suspended in 50 mL of H_2O_2 (10 mM) in a quartz tube, and O_2 was bubbled for 30 min to obtain an O_2 equilibrated environment. Thereafter, the system was irradiated by simulated sunlight for 2 h, and the concentration of the remaining H_2O_2 was measured.

2.5. The apparent quantum yield (AQY) measurement

The AQY of the photocatalytic reaction was measured under the illumination of a Xe lamp (Newport 150 W) equipped with bandpass filters at 360 nm, 400 nm, 420 nm, 450 nm, 500 nm and 600 nm (FWHM: 10 ± 2 nm). Typically, 100 mg of the catalyst was dispersed into 100 mL of a 10 vol% IPA solution and sonicated for 5 min. Then, 15 mL of the above mixture was placed in a quartz cuvette (1 cm × 5 cm ×4.5 cm) and stirred with O_2 flow for 0.5 h. Subsequently, the quartz cuvette reactor was placed at a distance of 30 cm from the filter to perform the AQY experiment (Fig. S2, Supporting Information). At the same time, the light intensity was measured. During the photocatalytic experiment, O_2 was continually bubbled into the solution and the irradiation area was 3.14 cm^2. After 30 min, the absorption curve of mixed solution was detected by UV–vis spectroscopy, and the corresponding relationship between the absorption peak and the concentration of the H_2O_2 solution was obtained.

According to the average amount of H_2O_2 produced by the photocatalytic reaction in 30 min, AQY is calculated as follows:

$$\eta_{AQY} = \frac{N_e}{N_p} \times 100\% = \frac{2 \times n \times N_A}{\frac{E_{total}}{E_{photon}}} \times 100\%$$

$$= \frac{2 \times n \times N_A}{\frac{S \times P \times t}{h \times \frac{c}{\lambda}}} \times 100\% = \frac{2 \times n \times N_A \times h \times c}{S \times P \times t \times \lambda} \times 100\%$$

Where, n is the amount of H_2O_2 molecules (mol), N_A is Avogadro constant (6.022×10^{23} /mol), h is the Planck constant (6.626×10^{-34} JS), c is the speed of light (3×10^8 m/s), S is the irradiation area (cm^2), P is the intensity of irradiation light (W/cm^2), t is the photoreaction time (s), λ is the wavelength of the monochromatic light (m).

2.6. First-principles calculations

Structural, electronic, and photocatalytic properties are calculated based on the Vienna ab initio Simulation Package (VASP) [32] using the generalized gradient approximation (GGA) along with the Perdew-Burke-Ernzerhof (PBE) functional. A van der Waals (vdW) interaction was described by the DFT-D3 method [33], and the Heyd-Scuseria-Ernzerhof hybrid functional (HSE06) was employed to calculate the electronic and optical properties [34]. A cutoff energy is set to 520 eV, and the structure is relaxed until the total energy and residual force reach 1×10^{-5}eV and 0.01 eV/Å, respectively. A $5 \times 5 \times 1$ *k*-point grid was used during the relaxation.

3. Results and discussion

The synthesis procedure of ACN is schematically shown in Fig. 1(a). The MCS obtained by dissolved melamine cyanuric acid in H_2SO_4 was used as a precursor, which served as a skeleton to maintain structural integrity. To fabricate hierarchical nanostructure ACN, the MCS powder

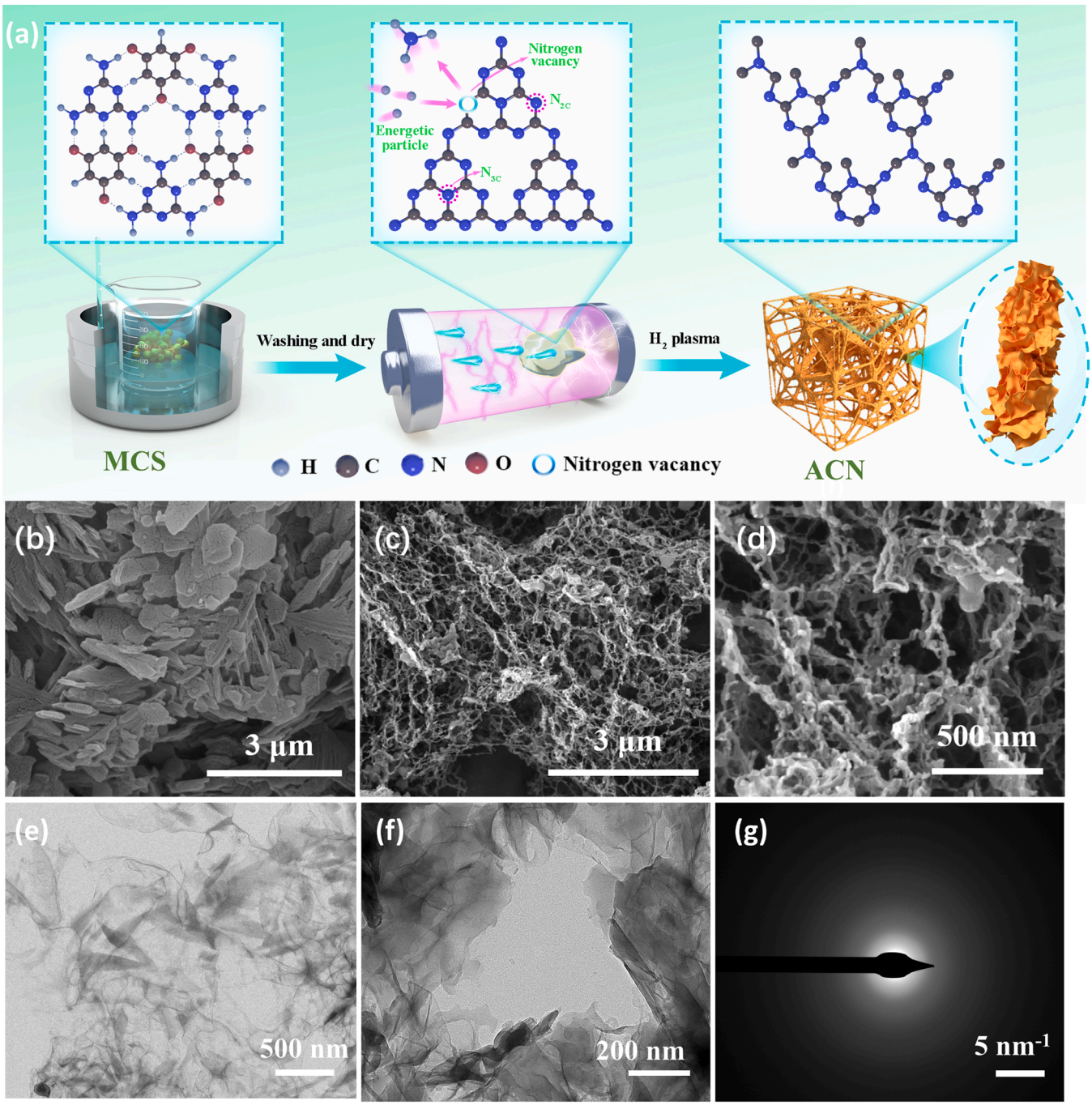

Fig. 1. (a) Schematic illustration of the synthesis of ACN, (b) SEM image of MCS, (c)-(d) SEM and (e)-(f) TEM images of ACN, and (g) SAED pattern of ACN.

was transferred to a tube furnace with H_2 plasma treatment, where H_2 plasma served as highly energetic particles bombarding the N lattice sites, accompanied by the release of NH_3, resulting in a continuous nanonetwork structure. Notably, the structure of ACN is assembled by nanosheets. SEM and TEM images were used to further confirm the successful formation of hierarchical continuous nanonetwork@nanosheet nanostructures. From Fig. 1(b)-(f), it can be concluded that the hierarchical nanostructure of ACN can be formed due to the bombardment of energetic particles from H_2 plasma. Selected area electron diffraction (SAED) recorded over μm^2 sized area reflect no crystal diffraction spot, indicating the amorphous structure of ACN shown in Fig. 1(g). To highlight the advantages of H_2 plasma treatment and hierarchical nanonetwork@nanosheet nanostructures, GCN was also prepared using MCS as a precursor in a muffle furnace, as shown in Fig. S3, Supporting Information. From the results, the GCN sample formed a continuous micronetwork but not a hierarchical structure with nanosheets, indicating that H_2 plasma treatment can efficiently create a hierarchical structure owing to the high-energy particles. As we know, the unique hierarchical structure can efficiently enhance the specific surface area of photocatalysis, thus promoting more active sites to occur in the reaction. A BET surface area of 405.758 m^2g^{-1} and a pore volume of 0.504 m^3g^{-1} are achieved on ACN, which are larger than those of GCN (29.416 m^2g^{-1}, 0.084 m^3g^{-1}) and BCN (4.891 m^2g^{-1}, 0.029 m^3g^{-1}), as shown in Table S2, Supporting Information. Moreover, all photocatalysts show similar nitrogen adsorption-desorption isotherms, which can be categorized as type IV isotherms according to the IUPAC classification shown in Fig. 2(a), indicating a large pore and middle well structure. From the porous structure (inter in Fig. 2(a)), the average pore diameter of ACN is ~7 nm, while that of GCN is ~2.5 nm. It is worth mentioning that H_2 plasma treatment can not only form a hierarchical structure but also significantly increase the specific surface area.

XRD patterns were used to identify the crystal structure of ACN. In Fig. 2(b), ACN shows distinctively different XRD patterns when compared to the samples of BCN and GCN. Obviously, the two typical characteristic diffraction peaks located at 13.1° and 27.5° correspond to the (100) and (002) planes of CN, which are attributed to the in-plane repeating heptazine structure and the interplanar stacking of aromatic systems, respectively. However, the two sharp peaks disappeared in ACN, which indicates long-range order disorder in the atomic arrangement [21] There is only one broad and flat peak near 24° in ACN, which preliminarily indicates the successful formation of amorphous carbon nitride. However, the possibility of forming (nitrogen-doped) carbon-like materials should be fully considered before concluding that the ACN sample exclusively consists of an amorphous structure. Carbon materials have two typical bands named the D and G bands located at approximately 1320 cm^{-1} and 1590 cm^{-1} in Raman spectra. In Fig. 2 (c), all samples show very similar Raman spectra without the D and G bands of carbon materials, suggesting the successful formation of amorphous carbon nitride [21]. The O peaks are located at 1058 and 1118 cm^{-1} shown in Fig S4(a), which can be ascribed to the asymmetric vibration and the out-of-phase stretching vibration of C-O-C bond, respectively [5]. However, the O peaks cannot be distinguished over ACN photocatalyst in the Raman spectrum due to the noise signal. Therefore, the FT-IR spectra and other characterizations were used to further explore the O-containing and surface groups.

In Fig. 2(d) and Fig. S4(b) (Supporting Information), the peaks located at 3000–3550 cm^{-1} can be ascribed to the tensile vibration of N-

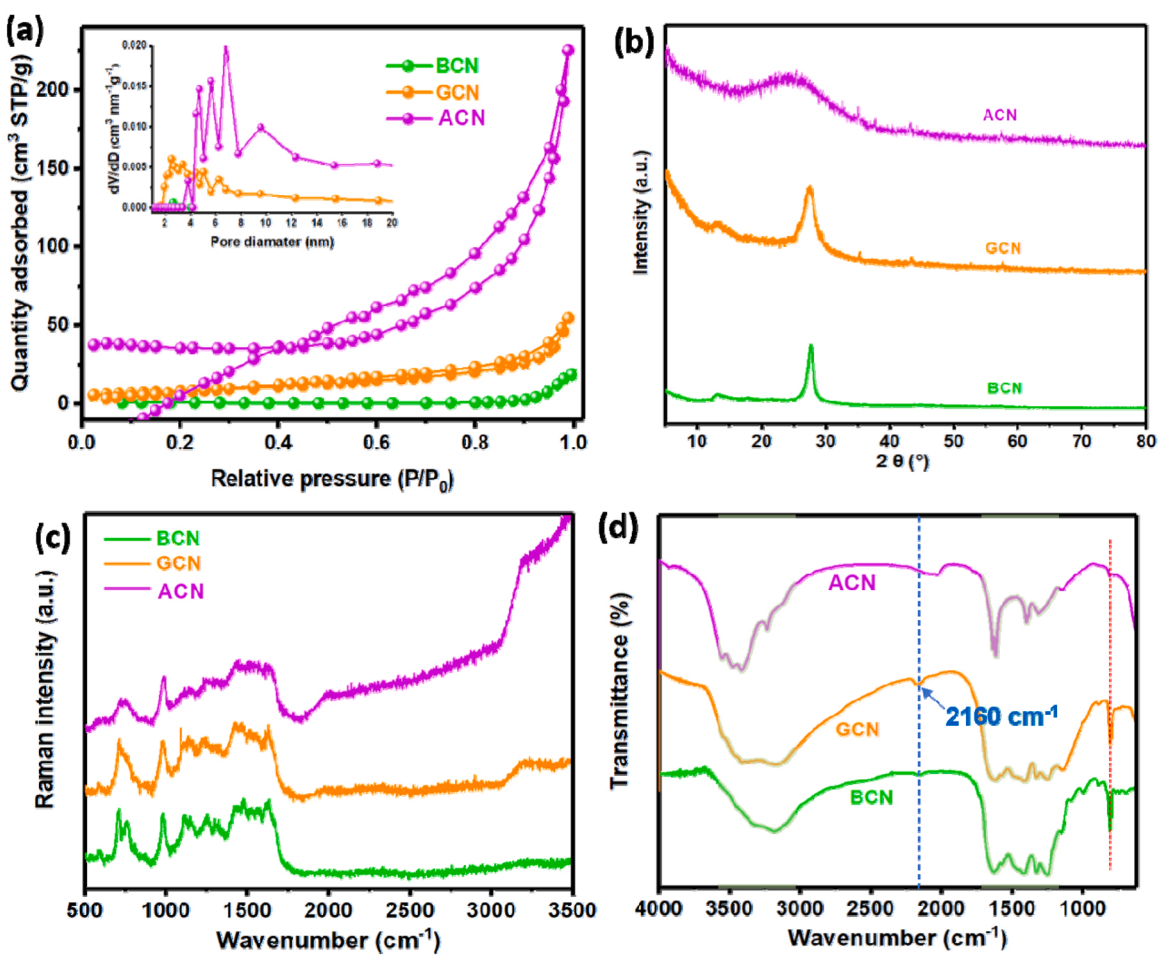

Fig. 2. (a) N_2 sorption isotherm, (b) XRD spectra, (c) Raman spectra excited by a 325 nm laser and (d) FT-IR spectra of BCN, GCN and ACN.

H and O-H, related to the unpolymerized N-H and absorbed H_2O molecules during the thermal polymerization process [35]. Compared with GCN, the newly generated peak at 3236 cm^{-1} of ACN is attributed to the N—H bond, and the peaks located at 3300–3550 cm^{-1} assigned to the surface -OH group are more obvious in ACN, which is caused by the H_2 plasma treatment. Highly nitrogen deficient is bacteria more easily to adsorb oxygen to stabilize the deficient structure [36]. Notably, another newly generated peak at 1620 cm^{-1} is assigned to be C═C bonds, indicating the presence of N vacancies. Moreover, the stretching mode of CN heterocycles in 1100–1700 cm^{-1} can be observed. However, the ACN sample has fewer peaks at 1100–1700 cm^{-1}, indicating disordered or amorphous components [37]. The peak at 810 cm^{-1} originates from the typical breathing mode of the tri-s-triazine ring. Notably, the smallest peak intensity for ACN indicates that the unique atomic arrangement of short-range order would be destroyed due to the energy particles from H_2 plasma treatment. The newly generated weak peak at

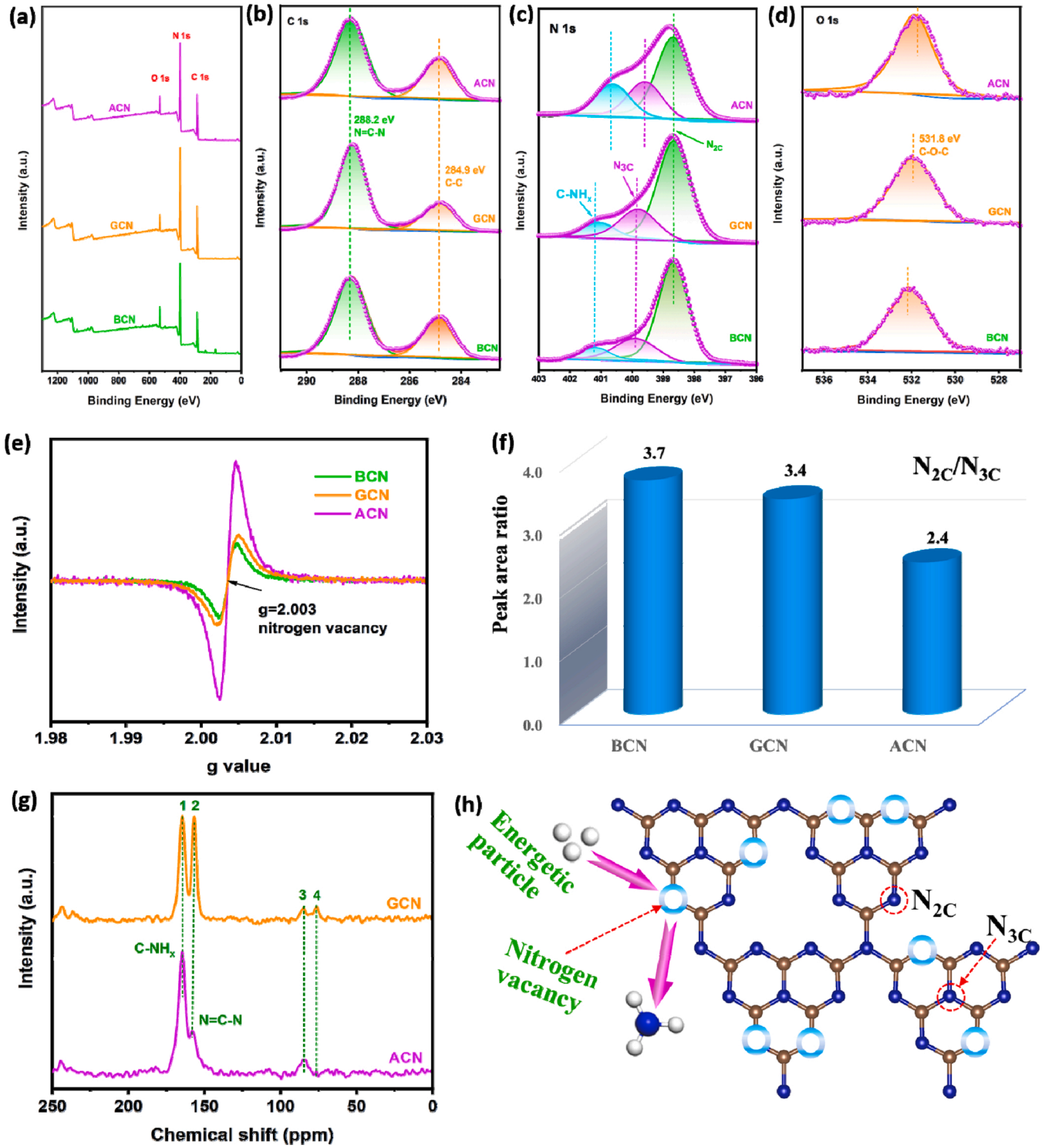

Fig. 3. XPS spectra of BCN, GCN, and ACN: (a) survey spectrum, (b)-(d) high-resolution XPS spectra of C 1 s, N 1 s, and O 1 s, (e) EPR spectra and (f) the peak area ratio of $N_{2\,C}$ to $N_{3\,C}$ groups of BCN, GCN and ACN, (g) ^{13}C solid-state MAS NMR spectra of ACN and GCN, (h) the model structure of different two $N_{2\,C}$ vacancies in one CN unit.

approximately 2160 cm^{-1} in GCN is assigned to the terminal cyano groups (-C≡N) [35]. Thus, the H_2 plasma treatment may destroy the lattice sites of tris-s-triazine with a typical short-range orderly structure [21]. To investigate the chemical states and element compositions of ACN in more detail, XPS spectra were employed. The survey spectrum suggests the presence of C, N, and O elements in all photocatalysts shown in Fig. 3(a). In Fig. 3(b), the high-resolution spectrum of the C 1 s peak can be deconvoluted into two peaks at 284.9 and 288.2 eV, which are assigned to the C-C group and the sp^2-bonded aromatic structure (N=C-N), respectively. The areas of ratio of the two peaks were similar for BCN, GCN and ACN, indicating that the carbon lattice site of CN was not destroyed [38]. Moreover, the N 1 s peaks (Fig. 3(c)) of ACN and GCN can be divided into three peaks located at approximately 398.8, 400.0 and 401.2 eV, corresponding to the functional groups of C-N=C (sp^2-hybridized nitrogen, $N_{2\,C}$), N-$(C)_3$ (sp^3-hybridized nitrogen, $N_{3\,C}$) and C-NH_x, respectively. It must be noted that the N-$(C)_3$ peak of ACN negatively shifts to 399.6 eV, with a shift of + 0.2 eV, compared to GCN. This suggests that the electronic structure of N-$(C)_3$ is changed in ACN because of structural defects (nitride vacancies) [39,40]. Meanwhile, the high-resolution spectra of O 1 s (Fig. 3(d)) show that one peak located at 531.8 eV is assigned to C-O-C [26], which is the result of O refilling [36]. The high content nitrogen vacancies in ACN photocatalyst are thermodynamically unstable, and the refilling oxygen in ACN (O-ACN) can be more stable. In Table S3, the O atom contents on ACN shows a slight increase after having been exposed to air for 3 months, while GCN remains unchanged. Moreover, the total energy of BCN, ACN and O-ACN are calculated to understand the effect of nitrogen vacancies and oxygen refilling on the structural stability. As shown in Fig. S5, the total energy of BCN is − 118.2 eV. When losing two $N_{2\,C}$-site atoms, the total energy of ACN is − 98.3 eV. After refilling with oxygen atoms at vacancy sites, the corresponding total energy is reduced to − 112.4 eV. Such lower total energies indicate that the oxygen refilling at the nitrogen vacancies can stabilize the structure.

Notably, the high-resolution XPS spectra are similar except for the N 1 s spectra. Thus, it can be concluded that structural defects may occur at the N lattice sites of tris-s-triazine. Therefore, electron paramagnetic resonance (EPR) spectroscopy was further used to verify the relationship between nitrogen vacancies concentration and unpaired-electrons in ACN. As shown in Fig. 3(e), a single Lorentzian line with a g value of approximately 2.003 was observed, indicating that ACN, GCN and BCN contain only one kind of paramagnetic species. According to the study of Xie group [41], this paramagnetic species of the ACN may be from the unpaired electrons in the localized π-conjugated structure, which can be assigned to the nitrogen vacancy. It is noted that the intensity of EPR signal over the ACN is higher than that of GCN, which is attributed to more defects in nanostructured ACN than GCN, suggesting a higher concentration of nitrogen vacancies as well as an increase in the number of unpaired electrons. Very interestingly, based on the atom contents derived from XPS analysis shown in Table S4 (Supporting Information), the surface N/C atom ratio was calculated as 0.98 for ACN, which is lower than the theoretical value (1.33) of ideal CN. Furthermore, the N/C atom ratio was also calculated by element analysis, which showed a value of 0.9783, indicating the introduction of nitride vacancies [42]. In addition, in the C 1 s spectra, the similar normalized absorbances for the C-C bond and C-N_3 bond indicate that there was no obvious change in the content of C. This result further supports the formation of nitrogen vacancies but not the increase in carbon vacancies. [38] To further clarify the change in each bonding state caused by H_2 plasma treatment, we conducted a detailed analysis of the N 1 s spectra, and the results are summarized in Table S5 (Supporting Information). It can be observed that the percentage of $N_{2\,C}$ decreases from 70.2% for BCN to 55.5% for ACN, indicating the construction of $N_{2\,C}$ vacancies [43]. Notably, compared to GCN and BCN, the percentage of $N_{3\,C}$ for ACN is basically unchanged. Moreover, the ratio of the peak area of $N_{2\,C}/N_{3\,C}$ is sharply decreased in ACN, suggesting that nitrogen vacancies are located at the $N_{2\,C}$ lattice sites [44].

Combining the abovementioned XPS spectra and EPR with FT-IR spectra, especially at an N/C atom rate of nearly 1, it can be concluded that H_2 plasma can introduce two $N_{2\,C}$-site nitrogen vacancies into one CN matrix. To further confirm this case, solid-state ^{13}C MAS NMR spectra were also recorded, as shown in Fig. 3(g). The signals at approximately 156.5 and 164.5 ppm are assigned to the C atoms in melem from a poly(tri-*s*-triazine) structure characteristic of N=C-N bonds and C-NH_x bonds, respectively [45,46]. In addition, compared to GCN, peak (2) of ACN is drastically reduced, while peak (1) remains the same, indicating the existence of nitrogen vacancies, which is consistent with the above results. To further explore the number of nitrogen vacancies, the integral area ratios within the solid-state ^{13}C NMR spectra of GCN and ACN were analyzed, as depicted in Table S6. The peak area of C-NH_x was normalized to 1.00. The N=C-N peak area of GCN is 0.75, which is approximately 2 times that of ACN (0.32), indicating that the number of N=C-N bonds in ACN is 2 times less than that in GCN. Thus, we can conclude that H_2 plasma can introduce two $N_{2\,C}$-site nitrogen vacancies in one CN matrix. Obviously, compared to GCN, the peak (4) located at approximately 76.3 ppm ascribed to -C≡N bonds in ACN disappears, which corresponds exactly to the result of the absence of -C≡N in ACN of FT-IR.

It is difficult to determine the structure of ACN due to the disorder of the amorphous structure. However, the amorphous state has long-range disorder and short-range order; thus, it is meaningful to determine the short-range structure of ACN. Therefore, we use first-principles calculations to illustrate the structural (the type of N vacancies of ACN) and electronic and optical properties of ACN and BCN. Fig. S6 (Supporting Information) shows the structure models and bandgap with different N vacancies. It can be seen from the results that the location and number of N vacancies have a significant impact on the band gap of CN. When the content of nitrogen vacancies is high, the structure of CN is severely damaged, which shows metallic characteristics. Moreover, by comparing the structure model and the concerning bandgap structure, it can be found that the cases where N vacancies occur on two adjacent $N_{2\,C}$ lattice sites are reasonable, and their band gaps are relatively stable at ~1 eV. Therefore, we can conclude that such structures (Zone 1 in Fig. S6) with two adjacent $N_{2\,C}$ vacancies are the most existing structures on the ACN and can be used as a structural model to perform first-principles calculations for the ACN. To verify the rationality of the utilized models, the more detail FT-IR spectra were checked out shown in Fig. S4(b) and Table S7 (Supporting Information). The peaks located at 1237–1636 cm^{-1} were assigned to the stretching vibration modes of heptazine heterocyclic ring (C_6N_7) units, which disappeared in ACN. However, the peak at 1398 cm^{-1} assigned to the C–N stretching of the tertiary nitrogen atoms in the middle of the carbon nitride structure can be observed both in BCN and ACN, which indicates that the $N_{3\,C}$ lattice site are not destroyed. Moreover, the absence peaks located at 1204–1306 cm^{-1} assigned to the Secondary bridging N in the ACN, indicating the destroyed of $N_{2\,C}$ lattice site. Thus, it can be concluded that the utilized models of ACN is fully consistent with the experimental result. Notably, the bandgap of BCN is 1.18 eV (under the PBE functional), which is consistent with the previously reported literature [47, 48]. However, the bandgap (Fig. S7) calculated by the ordinary functional GGA-PBE has a large deviation from the experimental value. Thus, the hybrid functional HSE06 was used to further investigate its electronic and optical properties. As shown in Fig. 4(a), the band gap of BCN is 2.73 eV, which is consistent with the previously reported literature [49] and is fully consistent with the experimental value of 2.72 eV shown in Fig. 4(c), indicating that the HSE06 method is reliable. According to the above results, we chose structure A (Supporting Information, Zone 1 in Fig. S6) as the structure model for ACN, which shows the narrowed bandgap of 1.55 eV shown in Fig. 4(b). Importantly, the experimental value of ACN is 2.24 eV, which has a deviation between the calculated values. The main reason for this deviation is that the structure on ACN does not all include structure A. Due to the random bombardment of energetic particles in H_2 plasma, ACN shows structural

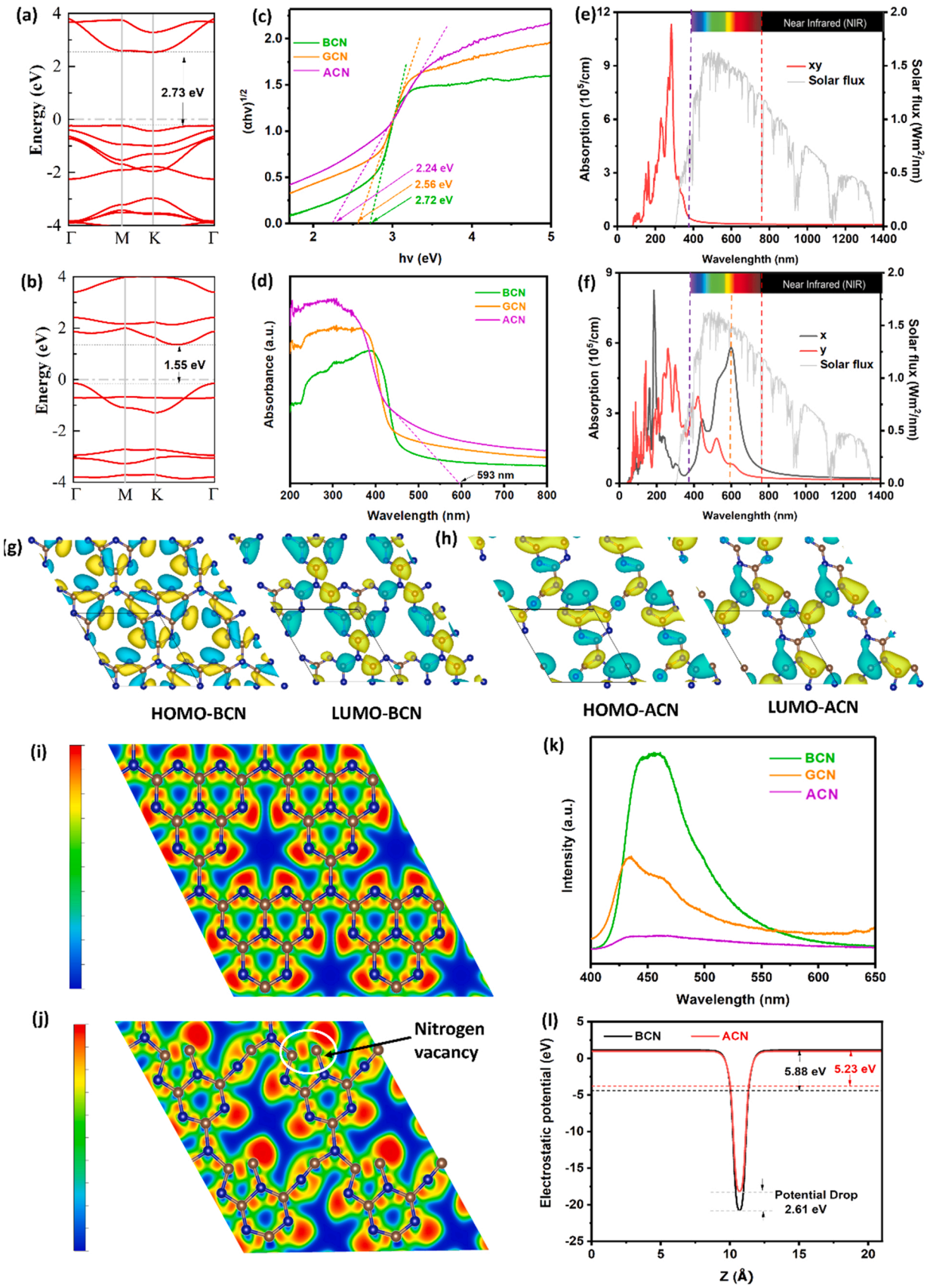

Fig. 4. (a)-(b) The band structures for BCN and ACN calculated by the HSE06 method. (c) Plots of $(\alpha h\nu)^{1/2}$ versus $h\nu$ and (d) UV–vis light absorption spectra of BCN, GCN, and ACN. (e)-(f) Optical absorption along the *x* and *y* directions, (g)-(h) The particle charge density (isosurface value of 3 e/Å^3) for BCN and ACN, respectively; (i)-(j) the electronic location function (ELF) of BCN and ACN, respectively; (k) The photoluminescence (PL) spectra of BCN, GCN, and ACN. (l) Potential drop across the interface of BCN and ACN.

defects with different N vacancies, and structure A is the majority among them. Compared to GCN (2.56 eV), ACN has a narrowed bandgap, indicating that the two $N_{2\,C}$ vacancies on ACN can efficiently reduce the bandgap, thus enhancing light absorption. Although many studies mention quantum size effect for nanomaterials, the bandgap over ACN is small due to the presence of defects in the structure, which is consistent with the theoretical calculation results. From the UV–vis light absorption spectra (Fig. 4(d)), ACN shows an increase in ultraviolet light absorption and possesses an absorption edge at approximately 468 nm. Interestingly, a long tail can be observed at the visible region for ACN, which originates from the amorphous transformation [22]. As a proof, the optical absorption of BCN and ACN was performed, as shown in Fig. 4(e) and 4(f), respectively. The ACN displays the ability to absorb sunlight absorption over a wide range in the visible and NIR regions. Strikingly, an asymmetric structure leads to anisotropic optical absorption along the *x*- and *y*-directions. A high absorption peak appears in the visible region at approximately 598 nm along the x-direction, which is consistent with the experimental test of the long tail absorption edge at 593 nm (Fig. 4(d)). Therefore, it can be concluded that the $N_{2\,C}$ vacancies caused n–π * electronic transitions, resulting in a smaller band gap and anisotropic optical properties.

Importantly, one can gain a comprehensive understanding of the electronic properties from the partial charge densities of the lowest unoccupied molecular orbital (LUMO) and highest occupied molecular

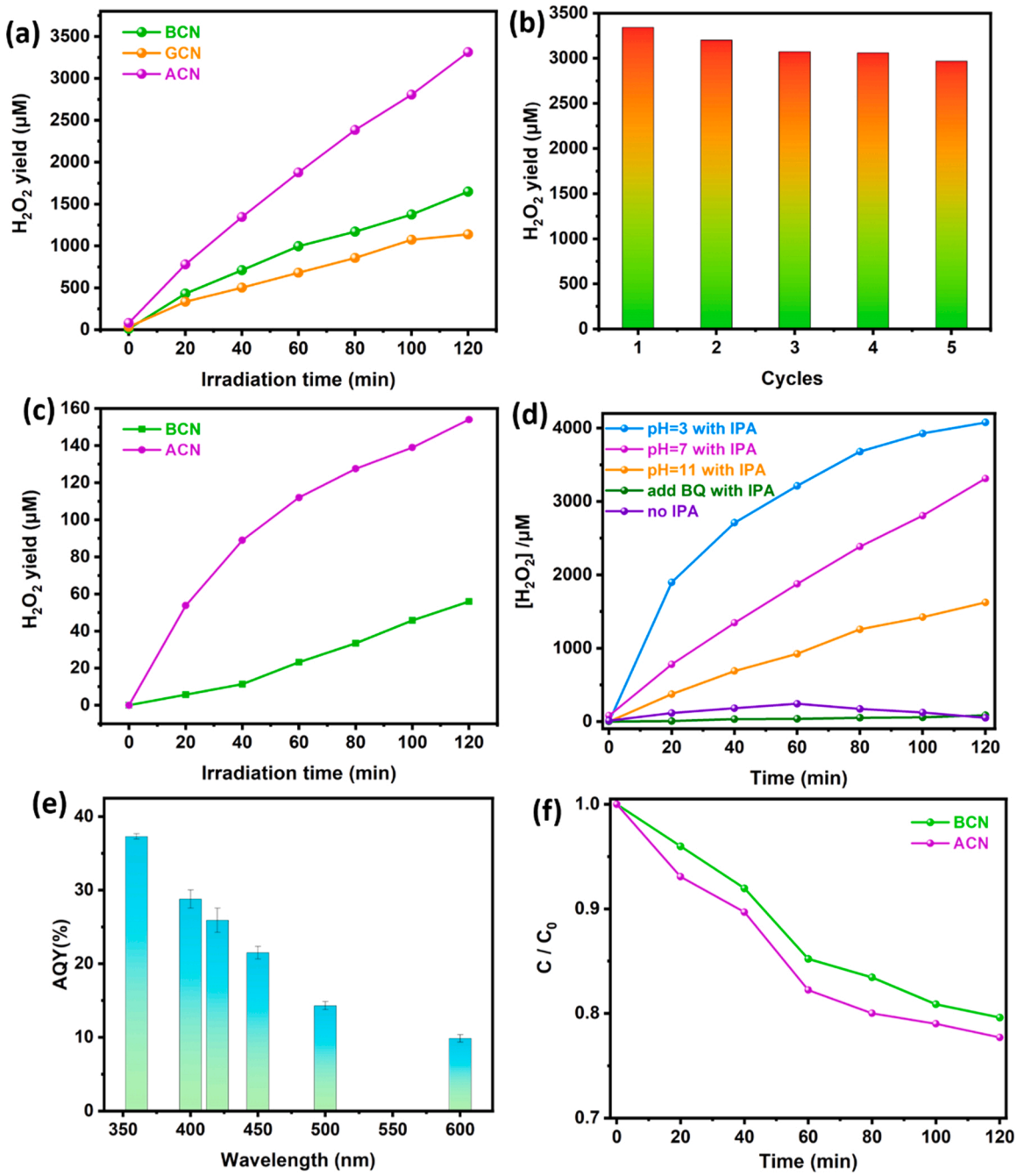

Fig. 5. (a) The photocatalytic H_2O_2 production on the BCN, GCN, and ACN under simulated solar irradiation; (b) H_2O_2 yield over ACN under 5 cycles using simulated solar irradiation; (c) the photocatalytic H_2O_2 production under visible light ($\lambda \geq 420$ nm); (d) the influence of PH, IPA and BQ during the H_2O_2 production on the ACN under simulated solar irradiation (pH is adjusted by HCl and KOH); (e) AQY of the ACN for the photocatalytic H_2O_2 production; (f) the photocatalytic decomposition of H_2O_2 over the ACN, the initial concentration of H_2O_2: 10 mM, Xe lamp.

orbital (HOMO), which are shown in Fig. 4(g) and (h) for BCN and ACN, respectively. Moreover, the electronic location function (ELF) of BCN and ACN are shown in Fig. 4(i) and (j). Obviously, the electrons are uniformly delocalized on the heptazine ring of BCN, while for ACN, the charges are redistributed owing to the asymmetrical structure, resulting in a certain electron-rich area on the nitrogen vacancy region [22,50]. Moreover, the ELF from the aspect of the (0 0 1) plane of ACN, which can show the bonding behavior, is also depicted in Fig. 4(j). The value of the ELF ranges from 0 to 1, denoted by blue to red color. Typically, the red color corresponds to perfect localization [51]. Comparing Fig. 4(i) with (j), an electronic local area appears near the N vacancy, indicating electron accumulation. The ELF is as high as 0.92 for ACN, which demonstrates the existence of strong covalent bonding between carbon atoms. As a proof, the ACN with one nitrogen vacancy, such as $N_{2\,C}$ and $N_{3\,C}$ in one CN unit, was also calculated by the hybrid functional HSE06 in Fig. S8-S9, Supporting Information. Obviously, ACN with one nitrogen vacancy is not reasonable owing to the conductor characteristic bandgap.

Theoretically, amorphous materials usually have rapid recombination of photogenerated electron-hole pairs due to the lack of a long-range ordered structure. However, our current work is not the case. As shown in Fig. 4(k), ACN has almost no PL peak, indicating the highest separation efficiency of photogenerated electron-hole pairs. To further study the reasons for the increased separation efficiency, a plane-averaged electrostatic potential drop was performed. We use the potential drop across the interface of BCN and ACN to describe the interface for ACN because of the existence of the original structure and amorphous structure in ACN. In Fig. 4(l), the potential drop across the BCN and ACN interfaces is 2.61 eV, resulting in the formation of a built-in electric field, which can facilitate carrier migration. Thus, the recombination of the photogenerated electron-hole pairs can be effectively reduced [52], which is consistent with the PL results. Compared with BCN, the metal work function of ACN is 5.23 eV, indicating that electrons escape from the surface of ACN more easily, which is consistent with the result of the photocurrent below.

To verify the advantages of hierarchical and amorphous structures as well as two $N_{2\,C}$-site vacancies, photocatalytic H_2O_2 production tests were evaluated. The photocatalytic activity of ACN for H_2O_2 production was assessed in the presence of a 10% IPA aqueous solution under simulated solar irradiation using a 300 W Xe lamp as the light source. For comparison, the performance of BCN and GCN were also evaluated. As shown in Fig. 5(a), the photocatalyst of BCN only produced 1647.8 μmol of H_2O_2, indicating poor photocatalytic activity. For ACN, the H_2O_2 yields increased to 3312.2 μmol due to the hierarchical structure, which provided a high specific surface area. However, it must be noted that the H_2O_2 yields were greatly decreased by GCN (1137.4 μmol) compared to ACN. This is because ACN has a wide spectral response and a short electron transmission path, which is beneficial for light-driven H_2O_2 production. In Fig. S10(a), Supporting Information, it can be clearly observed that the H_2O_2 yields for ACN are approximately 2 times and 2.9 times those of BCN and GCN, demonstrating the benefit of its particular hierarchical structure. Moreover, the hierarchical continuous nanonetwork structure composed of nanosheets can effectively increase the specific surface area, which can enhance H_2O_2 production. In addition, nanosheets have a large number of active sites, providing numerous carrier transport channels. [53] As reported, nitrogen vacancies can effectively promote the lifetime of photogenerated carriers. [54] The synergistic effect of nitrogen vacancies and hierarchical amorphous structures makes ACN exhibit high performance in photocatalytic H_2O_2 production. Moreover, the H_2O_2 yield remained stable when the reaction time exceeded 4 h shown in Fig. S10(b), Supporting Information. For practical applications, cycle experiments were carried out for five successive reaction runs under the same conditions. The photocatalysts were centrifuged from the reaction solution, washed with pure water, and dried at 60 ℃ overnight. Fig. 5(b) shows the results, which confirm the acceptable reusability of the ACN photocatalyst. In the fifth run after 10 h, the output of H_2O_2 on the ACN catalyst was nearly 2966.5 μmol, which was approximately 89.6% of the output in the first run. In addition, a considerably decay of H_2O_2 generated on ACN photocatalyst in repeated experiments can be the result of some photocatalyst lost during separation and washing process. Moreover, structural characterization of ACN photocatalyst was performed by SEM, XPS and XRD spectra after cycling experiments. From Fig. S11(a) and (b) (Supporting Information), it can be concluded that the hierarchical nanostructure of ACN remains intact after 5 cycles photocatalytic production H_2O_2 tests, indicating the stable hierarchical nanostructure of ACN. To investigate the chemical states and element compositions of ACN after 5 cycles tests more detail, XPS spectra were employed. In Fig. S11(c), a new peak appeared at 286.4 eV after 5 cycles testing, which is assigned to the C═O bond. The newly generated C═O peak attributes to the adsorption O_2, which comes from the continuous bubbling of O_2 during the photocatalysis process. The N 1 s spectra are is basically the same before and after 5 cycles photocatalytic production H_2O_2 tests shown in Fig. S11(d). Moreover, the XRD spectra of ACN after 1–5 cycles tests (Fig. S11(e), Supporting Information) are similar, indicating the good cycle stability of the ACN photocatalyst.

The activity of ACN for photocatalytic H_2O_2 production under visible light irradiation ($\lambda \geq 420$ nm) was also tested. For comparison, the performance of BCN, as a reference catalyst, was also evaluated. In Fig. 5(c), the concentration of H_2O_2 for ACN is 112 μmol h^{-1}, which is ~5 times higher than BCN (23 μmol h^{-1}). Additionally, a few articles have reported CN with N vacancies for improving photocatalytic H_2O_2 production, which are listed in Table S8 (Supporting Information). This result indicates that our work has the highest photocatalytic H_2O_2 production under both simulated sunlight and visible light ($\lambda \geq 420$ nm).

Typically, the surface of CN mainly has the following reactions in the process of photocatalytic H_2O_2 production, which can be divided into two reaction paths: the two-step single-electron reaction and the one-step two-electron reaction. The two-step single-electron reaction is shown in Eqs. (1) - (2), while Eq. (3) is the one-step two-electron reaction.

$$O_2 + e^- \rightarrow \bullet O_2^- \quad (1)$$

$$\bullet O_2^- + e^- + 2\,H^+ \rightarrow H_2O_2 \quad (2)$$

$$O_2 + 2e^- + 2\,H^+ \rightarrow H_2O_2 \quad (3)$$

To verify the reaction pathway of photocatalytic H_2O_2 production for ACN, benzoquinone (BQ) was employed. According to a previous report, the $\bullet O_2^-$ scavenger of BQ has no effect on iodometry [55]. In Fig. 5(d), the production of H_2O_2 is severely suppressed when BQ is added, which indicates that $\bullet O_2^-$ is an essential intermediate in the reduction pathway. Therefore, it can be concluded that the reaction pathway of ACN mainly obeys the two-step single-electron reaction. Moreover, it can be clearly observed that the decreased H_2O_2 production performance in the absence of IPA. This is because that the IPA as a hole scavenger will cause hole accumulation, and significantly reduce the charge separation. To further confirm the critical role of protons in the photocatalytic H_2O_2 production reaction, the photocatalytic performance of the ACN photocatalyst was studied under different pH values, as shown in Fig. 5(d). The photocatalytic H_2O_2 production on ACN showed enhanced performance under acidic conditions; however, it showed poor photocatalytic activity under alkaline conditions. Notably, the AQY of the ACN photocatalyst was approximately 5.2% at 360 nm, 4.4% at 400 nm, and 3.8% at 420 nm, as shown in Fig. 5(e). The trend of AQY fits the UV–vis light absorption spectrum well.

Due to thermodynamic instability, there are two competing pathways for the formation and decomposition of H_2O_2 [39]. The formation and decomposition rate constants (k_f and k_d) were estimated by fitting the data of time-dependent profiles of H_2O_2 production [56] shown in Fig. S12(a) and 12(b). Compared to BCN, the k_f value of ACN increased from 10.224 to 18.562 μM min^{-1} and the k_d value decreased from 0.008

to 0.005 μM min^{-1}. To further check the H_2O_2 decomposition process, the photocatalytic decomposition of H_2O_2 experiment was conducted shown in Fig. 5(f). After 2 h of irradiation, approximately 23% of the H_2O_2 degraded on ACN. Compared with the BCN (21%), the ACN catalyst afforded a higher decomposition rate, which may be due to the changes in the electronic structure owing to the amorphous structure [57]. The small difference of H_2O_2 decomposition over BCN and ACN fits the k_d well.

It is accepted that the photocatalytic performance mainly involves three determined factors: light absorption, charge separation and transport, and surface reaction [58]. The specific surface area and species affect the adsorption of O_2 and the photocatalytic active sites, thereby influencing the surface reaction [59]. The increasing surface area can also improve light absorption due to scattering of visible light caused by multiple internal reflections inside the hierarchical continuous nanosheet network structure, resulting in enhanced photocatalytic activity. In order to examine the comparative stability of the adsorption systems, we further calculated the adsorption energies by following relationship:

$$E_{ad} = E_{adsorbed} - (E_{adsorbate} + E_{adsorbent}) \quad (4)$$

where $E_{adsorbed}$, $E_{adsorbate}$, and $E_{adsorbent}$ are the energies of the adsorption systems, adsorbate, and adsorbent, respectively. Based on this equation, a smaller energy indicates that the structure is more

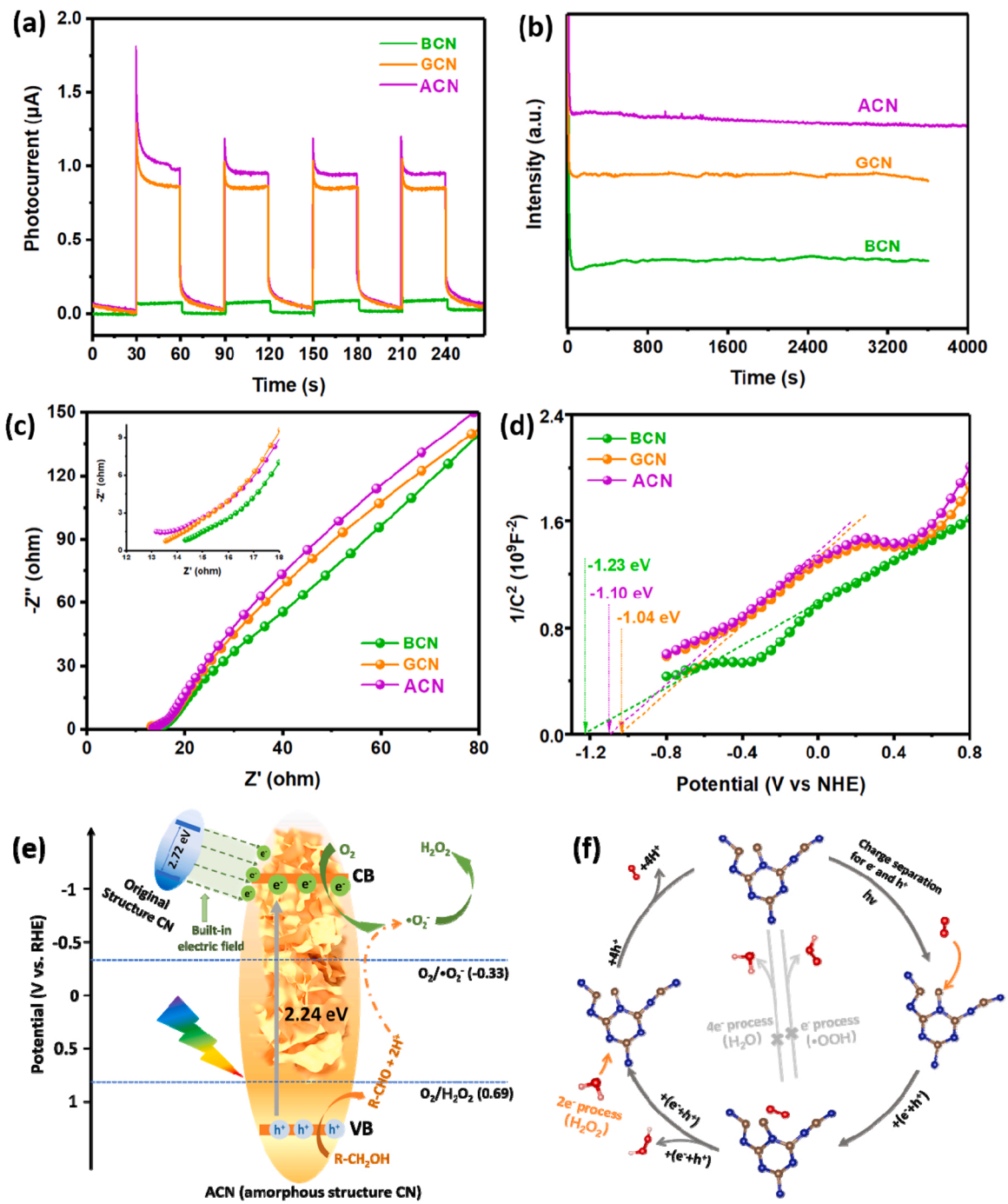

Fig. 6. (a) Transient photocurrent responses, (b) Chronoamperometry plot (i-t), (c) The electrochemical impedance spectra (EIS), (d) Mott-Schottky plots of BCN, GCN and ACN, (e) The band structure of ACN photocatalyst; (f) Mechanism of ACN photocatalytic H_2O_2 production.

energetically favorable. As shown in the Fig.S13, the O_2 binds more favorably on ACN than on BCN with a smaller energy of − 1.36 eV. To further investigate the O_2 adsorption for catalysts, the comparison of TPD-O_2 among BCN, GCN and ACN were shown in Fig. S14. The desorption of O_2 was observed in the lower (< 250 °C) and higher temperature (> 350 °C) regions, which is assigned to be physical adsorption and chemical adsorption, respectively. TPD-O_2 revealed that ACN exhibited the highest adsorption capacity of O_2, supporting the critical role of O_2 adsorption in the overall process. The preferred adsorption of O_2 can promote the two-step single-electron reduction of O_2 to H_2O_2.

Additionally, ACN also represents the highest photoelectrochemical performance (0.988 μA), which is ~13.7 and 1.2 times than that of BCN (0.072 μA) and GCN (0.849 μA), respectively, as shown in Fig. 6(a). The ACN sample exhibits excellent photocurrent stability when tested for a long reaction time under simulated sunlight, as shown in Fig. 6(b). To obtain more insight into the PEC performance, the electrochemical impedance spectra (EIS) and Mott-Schottky plots of BCN, GCN and ACN were measured, as shown in Fig. 6(c) and Fig. 6(d). It can be concluded that ACN has the lowest impedance, indicating the high efficiency of charge separation and transfer. The slopes of the linear region for Mott-Schottky are positive, demonstrating the n-type semiconductor [60].

Based on the above analysis of electronic structure, optical properties and photoelectrochemical performance, a possible photocatalytic H_2O_2 production mechanism of ACN can be proposed. As shown in Fig. 6(e), ACN harvests visible light to photoexcite electrons in VB to CB while leaving photogenerated holes in VB. On the one hand, the existence of the original structure and amorphous structure in ACN can form a built-in electric field, which can facilitate electron migration, thus promoting the accumulation of electrons on the surface of ACN. On the other hand, nitrogen vacancies create abundant unsaturated sites, resulting in a certain electron-rich area, which is conducive to O_2 adsorption. Then, $\bullet O_2^-$ is generated by the process of the oxygen reduction reaction. Meanwhile, proton donors of IPA are oxidized by holes. As a result, protons/$\bullet O_2^-$ can undergo surface redox reactions in the catalytic centers, producing H_2O_2. In summary, as shown in Fig. 6(f), the reaction pathway of ACN mainly obeys the two-step single-electron reaction to produce H_2O_2.

4. Conclusion

In summary, we report a one-step H_2 plasma treatment to induce a hierarchical amorphous CN (ACN) nanostructure with two $N_{2\ C}$-site vacancies in one unit of CN structure without element doping. Plasma-induced ACN is stable with a hierarchical continuous nanosheet network structure and exhibits an ultrahigh specific surface area and significantly enhanced photocatalytic H_2O_2 production. The two $N_{2\ C}$ vacancies located in one CN unit structure are determined by first-principles calculations and the consistent electronic character of experimental results and are indicated to reduce its band gap and thus to increase its light harvesting capacity. Moreover, the amorphous transformation leads to a new strong band tail, which remarkably enhances the absorbance edge of ACN, resulting in a wider range of visible-light absorption to enhance H_2O_2 production. The results have provided an effective approach for promoting the practical application of ACN in photocatalytic H_2O_2 production.

CRediT authorship contribution statement

Yanmei Zheng: Formal analysis, Conceptualization, Writing – review & editing, Data curation, Investigation, Methodology, Software, Validation. **Yi Luo:** Data curation, Methodology, Investigation, Software, Validation. **Qiushi Ruan:** Investigation, Analysis of research results. **Shaohua Wang:** Analysis of research results. **Jin Yu:** I Methodology, Software, Validation. **Xinli Guo:** Designer of the experiment, Editing, Supervision. **Weijie Zhang:** Analysis of research results. **Hang Xie:** Analysis of research results. **Zheng Zhang:** Analysis of research results. **Ying Huang:** Writing – review & editing.

Declaration of Competing Interest

The authors declare that they have no known competing financial interests or personal relationships that could have appeared to influence the work reported in this paper.

Acknowledgments

The authors would like to thank the financial support from the Jiangsu Key Science and Technology project (BE2019108), the National Natural Science Foundation of China (21173041), and the Opening Project of Jiangsu Key Laboratory of Advanced Metallic Materials, China.

Appendix A. Supporting information

Supplementary data associated with this article can be found in the online version at doi:10.1016/j.apcatb.2022.121372.

References

[1] D. Tang, C. Shao, S. Jiang, C. Sun, S. Song, Graphitic C2N3: an allotrope of g-C_3N_4 containing active azide pentagons as metal-free photocatalyst for abundant H_2 bubble evolution, ACS Nano 15 (4) (2021) 7208–7215.
[2] C. Cheng, B. He, J. Fan, B. Cheng, S. Cao, J. Yu, An inorganic/organic s-scheme heterojunction H_2-production photocatalyst and its charge transfer mechanism, Adv. Mater. 33 (22) (2021), e2100317.
[3] F. Chen, T. Ma, T. Zhang, Y. Zhang, H. Huang, Atomic-level charge separation strategies in semiconductor-based photocatalysts, Adv. Mater. 33 (10) (2021), e2005256.
[4] C. Bie, H. Yu, B. Cheng, W. Ho, J. Fan, J. Yu, Design, fabrication, and mechanism of nitrogen-doped graphene-based photocatalyst, Adv. Mater. 33 (9) (2021), e2003521.
[5] J. Li, B. Shen, Z. Hong, B. Lin, B. Gao, Y. Chen, A facile approach to synthesize novel oxygen-doped g-C3N4 with superior visible-light photoreactivity, Chem. Commun. 48 (2012) 12017–12019.
[6] G. Zhang, Y. Xu, C. He, P. Zhang, H. Mi, Oxygen-doped crystalline carbon nitride with greatly extended visible-light-responsive range for photocatalytic H_2 generation, Appl. Catal., B (2021) *283*.
[7] S.J. Phang, J.M. Goh, L.L. Tan, W.P.C. Lee, W.J. Ong, S.P. Chai, Metal-free n/n-junctioned graphitic carbon nitride (g-C_3N_4): a study to elucidate its charge transfer mechanism and application for environmental remediation, Environ. Sci. Pollut. Res. Int. 28 (4) (2021) 4388–4403.
[8] Y. Wang, R. Godin, J.R. Durrant, J. Tang, Efficient hole trapping in carbon Dot/Oxygen-modified carbon nitride heterojunction photocatalysts for enhanced methanol production from co2 under neutral condition, Angew. Chem. Int. Ed. 60 (38) (2021) 20811–20816.
[9] X. Chen, J. Wang, Y. Chai, Z. Zhang, Y. Zhu, Efficient photocatalytic overall water splitting induced by the giant internal electric field of a g-C_3N_4 /rGO/PDIP Z-scheme heterojunction, Adv. Mater. (2021), e2007479.
[10] N. Rohaizad, C.C. Mayorga-Martinez, M. Fojtu, N.M. Latiff, M. Pumera, Two-dimensional materials in biomedical, biosensing and sensing applications, Chem. Soc. Rev. 50 (1) (2021) 619–657.
[11] Y. Wang, X. Liu, X. Han, R. Godin, J. Chen, W. Zhou, C. Jiang, J.F. Thompson, K. B. Mustafa, S.A. Shevlin, J.R. Durrant, Z. Guo, J. Tang, Unique hole-accepting carbon-dots promoting selective carbon dioxide reduction nearly 100% to methanol by pure water, Nat. Commun. 11 (1) (2020) 2531.
[12] H. Zhao, Z. Jiang, K. Xiao, H. Sun, H.S. Chan, T.H. Tsang, S. Yang, P.K. Wong, Photo-assisted separation of noble-metal-free oxidation and reduction cocatalysts for graphitic carbon nitride nanosheets with efficient photocatalytic hydrogen evolution, Appl. Catal., B (2021) *280*.
[13] Y. Huo, J. Zhang, Z. Wang, K. Dai, C. Pan, C. Liang, Efficient interfacial charge transfer of 2D/2D porous carbon nitride/bismuth oxychloride step-scheme heterojunction for boosted solar-driven CO_2 reduction, J. Colloid Interface Sci. 585 (2021) 684–693.
[14] J. Ran, T.Y. Ma, G. Gao, X.-W. Du, S.Z. Qiao, Porous P-doped graphitic carbon nitride nanosheets for synergistically enhanced visible-light photocatalytic H_2 production, Energy Environ. Sci. 8 (12) (2015) 3708–3717.
[15] S. Tonda, S. Kumar, S. Kandula, V. Shanker, Fe-doped and -mediated graphitic carbon nitride nanosheets for enhanced photocatalytic performance under natural sunlight, J. Mater. Chem. A 2 (2014) 19.
[16] J. Zhang, X. Chen, K. Takanabe, K. Maeda, K. Domen, J.D. Epping, X. Fu, M. Antonietti, X. Wang, Synthesis of a carbon nitride structure for visible-light catalysis by copolymerization, Angew. Chem. Int. Ed. 49 (2) (2010) 441–444.
[17] J. Zhang, G. Zhang, X. Chen, S. Lin, L. Mohlmann, G. Dolega, G. Lipner, M. Antonietti, S. Blechert, X. Wang, Co-monomer control of carbon nitride

semiconductors to optimize hydrogen evolution with visible light, Angew. Chem. Int. Ed. 51 (13) (2012) 3183–3187.
[18] M.Z. Rahman, P.C. Tapping, T.W. Kee, R. Smernik, N. Spooner, J. Moffatt, Y. Tang, K. Davey, S.-Z. Qiao, A benchmark quantum yield for water photoreduction on amorphous carbon nitride, Adv. Funct. Mater. 27 (39) (2017).
[19] Xiaobo Chen, Lei, Peter Y. Liu, Yu, S.S. Mao, Increasing solar absorption for photocatalysis with black hydrogenated titanium dioxide nanocrystals, Science 331 (2011) 746.
[20] UlrikeDiebold, The surface science of titanium dioxide. Sur.e Sci. Rep. 2003, 48, 53.
[21] Y. Kang, Y. Yang, L.C. Yin, X. Kang, G. Liu, H.M. Cheng, An amorphous carbon nitride photocatalyst with greatly extended visible-light-responsive range for photocatalytic hydrogen generation, Adv. Mater. 27 (31) (2015) 4572–4577.
[22] R. Zhang, P. Li, F. Wang, L. Ye, A. Gaur, Z. Huang, Z. Zhao, Y. Bai, Y. Zhou, Atomically dispersed Mo atoms on amorphous g-C_3N_4 promotes visible-light absorption and charge carriers transfer, Appl. Catal., B 250 (2019) 273–279.
[23] P. Chen, H. Wang, H. Liu, Z. Ni, J. Li, Y. Zhou, F. Dong, Directional electron delivery and enhanced reactants activation enable efficient photocatalytic air purification on amorphous carbon nitride co-functionalized with O/La, Appl. Catal., B 242 (2019) 19–30.
[24] J. Li, X. Liu, H. Che, C. Liu, C. Li, Facile construction of O-doped crystalline / non-crystalline g-C_3N_4 embedded nano-homojunction for efficiently photocatalytic H_2 evolution, Carbon 172 (2021) 602–612.
[25] X. Qu, S. Hu, P. Li, Z. Li, H. Wang, H. Ma, W. Li, The effect of embedding N vacancies into g-C_3N_4 on the photocatalytic H_2O_2 production ability via H_2 plasma treatment, Diam. Relat. Mater. 86 (2018) 159–166.
[26] X. Ji, X. Yuan, J. Wu, L. Yu, H. Guo, H. Wang, H. Zhang, D. Yu, Y. Zhao, Tuning the photocatalytic activity of graphitic carbon nitride by plasma-based surface modification, ACS Appl. Mater. Interfaces 9 (29) (2017) 24616–24624.
[27] X. Li, J. Zhang, F. Zhou, H. Zhang, J. Bai, Y. Wang, H. Wang, Preparation of N-vacancy-doped g-C_3N_4 with outstanding photocatalytic H_2O_2 production ability by dielectric barrier discharge plasma treatment, Chin. J. Catal. 39 (6) (2018) 1090–1098.
[28] Z. Zhu, H. Pan, M. Murugananthan, J. Gong, Y. Zhang, Visible light-driven photocatalytically active g-C_3N_4 material for enhanced generation of H_2O_2, Appl. Catal., B 232 (2018) 19–25.
[29] L. Shi, L. Yang, W. Zhou, Y. Liu, L. Yin, X. Hai, H. Song, J. Ye, Photoassisted construction of holey defective g-C_3N_4 photocatalysts for efficient visible-light-driven H_2O_2 production, Small 14 (9) (2018).
[30] Y. Ding, W. Zhao, H. Hua, B. Ma, [π-$C_5H_5N(CH_2)_{15}CH_3]_3[PW_4O_{32}]$/$H_2O_2$/ethyl acetate/alkenes: a recyclable and environmentally benign alkenes epoxidation catalytic system, Green. Chem. 10 (9) (2008).
[31] M. Saha, M. Das, R. Nasani, I. Choudhuri, M. Yousufuddin, H.P. Nayek, M. M. Shaikh, B. Pathak, S. Mukhopadhyay, Targeted water soluble copper-tetrazolate complexes: interactions with biomolecules and catecholase like activities, Dalton Trans. 44 (46) (2015) 20154–20167.
[32] K. Momma, F. Izumi, VESTA3for three-dimensional visualization of crystal, volumetric and morphology data, J. Appl. Cryst. 44 (6) (2011) 1272–1276.
[33] Grimme Stefan, Antony Jens, Ehrlich Stephan, H. Krieg, A consistent and accurate abinitio parametrization of density functional dispersion correction (DFT-D) for the 94 elements H-Pu, J. Chem. Phys. 132 (2010), 154104.
[34] J. Heyd, G.E. Scuseria, Hybrid functionals based on a screened Coulomb potential, J. Chem. Phys. 118 (2003) 8207–8215.
[35] D. Zhao, C.L. Dong, B. Wang, C. Chen, Y.C. Huang, Z. Diao, S. Li, L. Guo, S. Shen, Synergy of dopants and defects in graphitic carbon nitride with exceptionally modulated band structures for efficient photocatalytic oxygen evolution, Adv. Mater. 31 (43) (2019), e1903545.
[36] Q. Sun, Y. Wu, J. Zhu, C. Lu, Y. Sun, Z. Wang, J. Chen, Stabilizing plasma-induced highly nitrogen-deficient g-C3N4 by heteroatom-refilling for excellent lithium-ion battery anodes, Chem. Eng. J. 427 (2022), 131032.
[37] A. Vesel, I. Junkar, U. Cvelbar, J. Kovac, M. Mozetic, Surface modification of polyester by oxygen- and nitrogen-plasma treatment, Sur. Inter. Anal. 40 (11) (2008) 1444–1453.
[38] S. Li, G. Dong, R. Hailili, L. Yang, Y. Li, F. Wang, Y. Zeng, C. Wang, Effective photocatalytic H_2O_2 production under visible light irradiation at g-C_3N_4 modulated by carbon vacancies, Appl. Catal., B 190 (2016) 26–35.
[39] S. Zhao, X. Zhao, H. Zhang, J. Li, Y. Zhu, Covalent combination of polyoxometalate and graphitic carbon nitride for light-driven hydrogen peroxide production, Nano Energy 35 (2017) 405–414.
[40] R. Wang, X. Zhang, F. Li, D. Cao, M. Pu, D. Han, J. Yang, X. Xiang, Energy-level dependent H_2O_2 production on metal-free, carbon-content tunable carbon nitride photocatalysts, J. Energy Chem. 27 (2) (2018) 343–350.
[41] P. Xia, B. Cheng, J. Jiang, H. Tang, Localized π-conjugated structure and EPR investigation of g-C_3N_4 photocatalyst, Appl. Sur. Sci. 487 (2019) 335–342.
[42] H. Yu, R. Shi, Y. Zhao, T. Bian, Y. Zhao, C. Zhou, G.I.N. Waterhouse, L.Z. Wu, C. H. Tung, T. Zhang, Alkali-assisted synthesis of nitrogen deficient graphitic carbon nitride with tunable band structures for efficient visible-light-driven hydrogen evolution, Adv. Mater. 29 (16) (2017).
[43] Y. Duan, Y. Wang, L. Gan, J. Meng, Y. Feng, K. Wang, K. Zhou, C. Wang, X. Han, X. Zhou, Amorphous carbon nitride with three coordinate nitrogen (N3C) vacancies for exceptional NOx abatement in visible light, Adv. Energy Mater. 11 (19) (2021).
[44] G. Liu, G. Zhao, W. Zhou, Y. Liu, H. Pang, H. Zhang, D. Hao, X. Meng, P. Li, T. Kako, J. Ye, In situ bond modulation of graphitic carbon nitride to construct p-n homojunctions for enhanced photocatalytic hydrogen production, Adv. Funct. Mater. 26 (37) (2016) 6822–6829.
[45] J. Sun, J. Zhang, M. Zhang, M. Antonietti, X. Fu, X. Wang, Bioinspired hollow semiconductor nanospheres as photosynthetic nanoparticles, Nat. Commun. 3 (2012) 1.
[46] G. Ba, T. Huo, Q. Deng, H. Li, W. Hou, Mechanochemical synthesis of nitrogen-deficient mesopore-rich polymeric carbon nitride with highly enhanced photocatalytic performance, ACS Sustain. Chem. Eng. 8 (50) (2020) 18606–18615.
[47] J. Fu, B. Zhu, C. Jiang, B. Cheng, W. You, J. Yu, Hierarchical porous O-Doped g-C3 N4 with enhanced photocatalytic CO_2 reduction activity, Small 13 (15) (2017).
[48] L. Lin, H. Ou, Y. Zhang, X. Wang, Tri-s-triazine-based crystalline graphitic carbon nitrides for highly efficient hydrogen evolution photocatalysis, ACS Catal. 6 (6) (2016) 3921–3931.
[49] A. Du, S. Sanvito, Z. Li, D. Wang, Y. Jiao, T. Liao, Q. Sun, Y.H. Ng, Z. Zhu, R. Amal, S.C. Smith, Hybrid graphene and graphitic carbon nitride nanocomposite: gap opening, electron-hole puddle, interfacial charge transfer, and enhanced visible light response, J. Am. Chem. Soc. 134 (9) (2012) 4393–4397.
[50] M. Bafekry, M.M. Faraji, H.R. Fadlallah S. Jappor; M. Karbasizadeh, Ghergherehchi , D. Gogova, , Biphenylene monolayer as a two-dimensional nonbenzenoid carbon allotrope: A first-principles study. Material. Sci. 2021.
[51] M. Perveen, S. Nazir, A.W. Arshad, M.I. Khan, M. Shamim, K. Ayub, M.A. Khan, J. Iqbal, Therapeutic potential of graphitic carbon nitride as a drug delivery system for cisplatin (anticancer drug): a DFT approach, Biophys. Chem. 267 (2020), 106461.
[52] Y. Luo, S. Wang, K. Ren, J.P. Chou, J. Yu, Z. Sun, M. Sun, Transition-metal dichalcogenides/$Mg(OH)_2$ van der Waals heterostructures as promising water-splitting photocatalysts: a first-principles study, Phys. Chem. Chem. Phys. 21 (4) (2019) 1791–1796.
[53] L. Zhou, J. Feng, B. Qiu, Y. Zhou, J. Lei, M. Xing, L. Wang, Y. Zhou, Y. Liu, J. Zhang, Ultrathin g-C_3N_4 nanosheet with hierarchical pores and desirable energy band for highly efficient H_2O_2 production, Appl. Catal., B (2020) *267*.
[54] Y. Wang, D. Meng, X. Zhao, Visible-light-driven H_2O_2 production from O_2 reduction with nitrogen vacancy-rich and porous graphitic carbon nitride, Appl. Catal., B (2020) *273*.
[55] H. Xie, Y. Zheng, X. Guo, Y. Liu, Z. Zhang, J. Zhao, W. Zhang, Y. Wang, Y. Huang, Rapid microwave synthesis of mesoporous oxygen-doped g-C3N4 with carbon vacancies for efficient photocatalytic H_2O_2 production, ACS Sustain. Chem. Eng. 9 (19) (2021) 6788–6798.
[56] A. Torres-Pinto, M.J. Sampaio, C.G. Silva, J.L. Faria, M.T. Silva A, Recent strategies for hydrogen peroxide production by metal-free carbon nitride photocatalysts, Catalysts 9 (2019) 12.
[57] R. Wang, X. Zhang, F. Li, D. Cao, M. Pu, D. Han, J. Yang, X. Xiang, Energy-level dependent H_2O_2 production on metal-free, carbon-content tunable carbon nitride photocatalysts, J. Energy Chem. 27 (2018) 343–350.
[58] Z. Liu, G. Wang, H.S. Chen, P. Yang, An amorphous/crystalline g-C_3N_4 homojunction for visible light photocatalysis reactions with superior activity, Chem. Commun. (Camb.) 54 (37) (2018) 4720–4723.
[59] Y. Shiraishi, Y. Kofuji, H. Sakamoto, S. Tanaka, S. Ichikawa, T. Hirai, Effects of surface defects on photocatalytic H_2O_2 production by mesoporous graphitic carbon nitride under visible light irradiation, ACS Catal. 5 (5) (2015) 3058–3066.
[60] Y. Zheng, Y. Liu, X. Guo, W. Zhang, Y. Wang, M. Zhang, R. Li, Z. Peng, H. Xie, Y. Huang, In-situ construction of morphology-controllable 0D/1D g-C_3N_4 homojunction with enhanced photocatalytic activity, Appl. Sur. Sci. (2021) 563.